Combustion and Flame 222 (2020) 123–132

Contents lists available at ScienceDirect

Combustion and Flame

journal homepage: www.elsevier.com/locate/combustflame

Hydrogen migration as a potential driving force in the thermal decomposition of dimethoxymethane: New insights from pyrolysis imaging photoelectron photoion coincidence spectroscopy and computations

Tongpo Yu[a], Xiangkun Wu[a,b], Xiaoguo Zhou[a,c,*], Andras Bodi[b], Patrick Hemberger[b,**]

[a] Hefei National Laboratory for Physical Sciences at the Microscale, Department of Chemical Physics, University of Science and Technology of China, Hefei 230026, China
[b] Laboratory for Synchrotron Radiation and Femtochemistry, Paul Scherrer Institute, Villigen 5232, Switzerland
[c] National Synchrotron Radiation Laboratory, University of Science and Technology of China, Hefei 230029, China

ARTICLE INFO

Article history:
Received 8 May 2020
Revised 21 August 2020
Accepted 23 August 2020

Keywords:
Methylal
Pyrolysis
PEPICO
Photoelectron spectroscopy
Kinetics

ABSTRACT

Pyrolysis and low-temperature oxidation of dimethoxymethane (methylal, $MeOCH_2OMe$) play an important role in the ignition of blended diesel fuels, but the underlying mechanisms are still debated. In these kinetic models, bimolecular hydrogen abstraction or unimolecular C–O bond fission are considered as the primary initial steps, while $MeOCH_2OMe$ isomerization is sometimes disregarded. In this work, we investigate the pyrolysis of $MeOCH_2OMe$ combining imaging photoelectron photoion coincidence spectroscopy with vacuum ultraviolet (VUV) synchrotron radiation and CBS-QB3 theoretical calculations to unveil reaction paths and energetics. In the mass spectrum of $MeOCH_2OMe$, pyrolysis products and radical intermediates were observed at *m/z* 15 (CH_3), 28 (CO), 29 (HCO), 30 (H_2CO), 31 (CH_2OH), 32 (CH_3OH), 45 (CH_3OCH_2), and 75 (H-loss from methylal). Only the *m/z* 45 and 75 ions are found to be dissociative photoionization products of $MeOCH_2OMe$, the other mass spectral peaks are attributed to ionization of the neutral $MeOCH_2OMe$ pyrolysis products. The *m/z* 31 peak was assigned to the methoxy radical in the previous studies. However, our photoion mass-selected threshold photoelectron spectrum (ms-TPES) confirms that it originates from dissociative photoionization of the primary pyrolysis fragment methanol. Based on the experimental and computational results, a thermal decomposition mechanism of $MeOCH_2OMe$ is proposed. Here, H-migration precedes the production of methoxymethylene (CH_3OCH) and methanol, while dimethyl ether and formaldehyde are probably formed in multi-step processes, too. The sequential dissociation of CH_3OCH and of dimethyl ether yields enhanced *m/z* 15, 28 and 29 signals at high temperature. Rate constants have been calculated to confirm the dominant role of $MeOCH_2OMe$ isomerization and to help improve predictive combustion models.

1. Introduction

Oxygenated hydrocarbon additives are blended into gasoline and diesel fuels to reduce carbon monoxide and unburned hydrocarbon emissions [1–6]. Since the emission reduction is thought to be related to the C–O bonds in these oxygenates, oxymethylene ethers (OMEs) with the structure of $CH_3–O–(CH_2–O)_n–CH_3$ are promising biofuel additives, similar to alcohols and ethers. In view of atmospheric pollution, the positive influence on the soot–NO_x trade-off makes blending OMEs into diesel fuels appealing worldwide [7–11]. It was found that blends of more than 15% reduced the formation of particulate matter (soot) by up to 52% and NO_x by 4% compared to common diesel fuels [12,13].

Dimethoxymethane ($MeOCH_2OMe$ or methylal) is the simplest OME, has a low boiling point and cetane number (CN = 29) [9]. The CN reflects on fuel ignition properties, which is why understanding the low-temperature pyrolysis and oxidation kinetics of $MeOCH_2OMe$ is crucial for its rational application in fuels. To acquire an in-depth knowledge of $MeOCH_2OMe$ kinetics, experimental and theoretical investigations have been performed recently.

* Corresponding author at: Hefei National Laboratory for Physical Sciences at the Microscale, Department of Chemical Physics, University of Science and Technology of China, Hefei 230026, China.
** Corresponding author.
E-mail addresses: xzhou@ustc.edu.cn (X. Zhou), patrick.hemberger@psi.ch (P. Hemberger).

https://doi.org/10.1016/j.combustflame.2020.08.040
0010-2180/

In 2017, Kopp et al. [14] first elucidated the oxidation kinetics of $MeOCH_2OMe$ using high-level *ab initio* and statistical mechanics methods. Hydrogen abstraction from the terminal methyl or the central methylene groups of $MeOCH_2OMe$ by H atoms and CH_3 radicals was assumed to trigger oxidation kinetics and rate constants were calculated for these processes. Vermeire et al. [15] measured end products of the $MeOCH_2OMe$ oxidation and pyrolysis in an isothermal quartz jet-stirred reactor (JSR) with gas chromatography–mass spectrometry (GC–MS), and proposed a kinetic model with the aid of *ab initio* calculated thermodynamic properties and reaction rates. Sun et al. [16] probed reactive intermediates by combining a JSR and molecular-beam mass spectrometry as well as gas chromatography and Fourier transform infrared spectroscopy. A new kinetic model was constructed for the oxidation of $MeOCH_2OMe$, in which hydrogen abstraction by OH and CH_3 radicals or H atoms was still postulated to be the primary reaction prior to sequential decomposition and O_2-addition. Other thermal decomposition processes of $MeOCH_2OMe$ were not included in this model, either. Further analytical tools were applied by Peukert et al. in shock-tube experiments of $MeOCH_2OMe$ pyrolysis and oxidation in the 1100−1430 K temperature range [17], such as hydrogen atomic resonance absorption spectrometry (H-ARAS), high-repetition time-of-flight mass spectrometry (HR-TOF-MS) and GC–MS. Based on the results and the fact that C–O bond energies are lower than those of C–H bonds, the two C–O bond fission reactions of $MeOCH_2OMe$, (3) and (4), were suggested to be the primary initial reactions instead of C–H bond fissions, (1) and (2). As a result, large discrepancies in the experimental and theoretical product mole fractions could be explained qualitatively. However, the simulated end product ratios were still in sizeable disagreement with the measured results.

Peukert et al. [17] and Golka et al. [18] found that hydrogen atoms are formed by sequential dissociation of the radicals, which were produced during the initial reactions (3) and (4). Although it was impossible to clearly determine a branching ratio between the two possible C–O bond fissions, the concentration–time profiles of $MeOCH_2OMe$ and of the stable products, such as CH_4, CO, and CH_2O recorded in shock-tube experiments were reproduced with reasonable accuracy when both bimolecular H-abstraction and unimolecular C–O bond fission were included by in the original kinetic model [19]. Still, a significant question remains: Why is the C–O bond broken in reaction (3), although (4) is energetically favored?

$$CH_3OCH_2OCH_3 \rightarrow CH_2OCH_2OCH_3 + H \quad (1)$$

$$CH_3OCH_2OCH_3 \rightarrow CH_3OC(H)OCH_3 + H \quad (2)$$

$$CH_3OCH_2OCH_3 \rightarrow CH_3O + CH_2OCH_3 \quad (3)$$

$$CH_3OCH_2OCH_3 \rightarrow CH_3 + OCH_2OCH_3 \quad (4)$$

Golka et al. [20], adressed this question further by theoretical analysis on the branching ratio of C–O bond fissions. It is worth noting that no indication for additional reaction channels was found.

To our surprise, the isomerization–decomposition pathways of $MeOCH_2OMe$ itself have been rarely considered in the kinetic models [15–19]. He et al. assumed the reaction of $MeOCH_2OMe \rightarrow CH_3OCH_3 + H_2CO$ as the primary pathway in the $MeOCH_2OMe$ combustion [21], while in the $MeOCH_2OMe$ ignition study of Jacobs et al. [22], another complex fragmentation pathway of $CH_3OH + HCO + CH_3$ was discussed together with the C–H, C–O bond fissions, and CH_3OCH_3 formation. However, neither discussed the mechanism and energetics of the $CH_3OCH_3 + H_2CO$ and $CH_3OH + HCO + CH_3$ reaction channels. In Hu et al.'s modeling study [23], this unimolecular decomposition reaction channel was found to be a fuel-specific chain initiation reaction. Moreover, it is worth noting that these previous combustion and pyrolysis experiments were conducted at atmospheric pressure. At elevated pressure, unimolecular processes may play a relatively subdued role in comparison with bimolecular hydrogen abstraction by fuel radicals [24].

It has been seen in the unimolecular decomposition of numerous, mid-sized organic species, such as dimethyl methylphosphonate [25] and resorcinol [26] that key products are formed in dissociation processes following isomerization steps, while simple bond scissions are often unfavorable. Furthermore, in cyclopentanone, H-migration was found to play a central role [27]. Therefore, we set out to determine the possible role of isomerization in the thermal decomposition of $MeOCH_2OMe$. Based on the pyrolysis results, we have considered the H-migration isomerization steps (5–8) and multigroup transfers (9–10) in particular.

$$CH_3OCH_2OCH_3 \rightarrow CH_3OH + trans - CH_3OCH \quad (5)$$

$$CH_3OCH_2OCH_3 \rightarrow CH_3OH + cis - CH_3OCH \quad (6)$$

$$CH_3OCH_2OCH_3 \rightarrow CH_3OH + CH_2OCH_2 \quad (7)$$

$$CH_3OCH_2OCH_3 \rightarrow CH_2O + CH_3OCH_3 \quad (8)$$

$$CH_3OCH_2OCH_3 \rightarrow CH_2O + CH_3CH_2OH \quad (9)$$

$$CH_3OCH_2OCH_3 \rightarrow CH_4 + HCOOCH_3 \quad (10)$$

Photoionization with VUV synchrotron radiation combined with imaging photoelectron photoion coincidence spectroscopy (*i*PEPICO) provides a snapshot of the pyrolysis process [25] and direct spectral evidence of reactive intermediates [28–36]. In this work, we have applied *i*PEPICO to study the unimolecular thermal decomposition of $MeOCH_2OMe$. By recording the photoion mass-selected threshold photoelectron spectra (ms-TPES), the key pyrolysis intermediates of $MeOCH_2OMe$ can be identified with the help of Franck–Condon simulations [37,38]. Moreover, the temperature-dependent behavior of the intermediates and products have been measured, as well. With the aid of the high-level quantum chemical calculations and kinetic modeling, a thermal decomposition mechanism is proposed for $MeOCH_2OMe$.

2. Experimental and computational methods

All experiments were carried out at the VUV beamline of the Swiss Light Source, Paul Scherrer Institute. Both the beamline and the imaging PEPICO spectrometer have been described in detail elsewhere [38–41]. In brief, a bending magnet generated VUV synchrotron radiation, which was collimated, dispersed by a grazing incidence monochromator with a 150 lines/mm blazed grating, and focused into a differentially pumped gas filter with the exit slit, after which it entered the ionization chamber of the *i*PEPICO endstation. The photon energy resolution was 6 meV at 8 eV. The gas filter was normally filled with a mixture of neon, argon and krypton at a pressure of 10 mbar over an optical length of 10 cm to suppress higher-order radiation above 14 eV. The absolute photon energy was calibrated using argon autoionization lines [29].

$MeOCH_2OMe$ (99%) was purchased from Sigma-Aldrich Inc. and used without further purification. To identify the dissociative pho-

toionization channels of the sample, mass spectra were recorded at room temperature, using an effusive source. A temperature-controlled Chen-type pyrolysis reactor [42] was applied to study the thermal decomposition of $MeOCH_2OMe$ at temperatures up to 1245 K. In the present microreactor experiment with supersonic expansion, the pressure in the reactor (resistively heated silicon carbide tube) was roughly a few tens of mbar, at a residence time of 10−100 μs. Once leaving the reactor, the gas mixture is expanded into the source chamber (10^{-4} mbar), where the mean free path was about 1 m. A gas mixture of 0.4% $MeOCH_2OMe$ in helium was prepared at a total pressure of 10 bar in a stainless-steel tank. This mixture was further diluted by a factor of ten using mass flow controllers, which yields a $MeOCH_2OMe$ concentration of 0.04% in the seed, effectively suppressing bimolecular chemistry in the ca. 3 cm long silicon carbide reactor with 1 mm internal diameter. The detailed experimental conditions are listed in Table S2 of the supporting information. Additionally, when the initial $MeOCH_2OMe$ concentration was increased to 0.33%, we observed trace amounts of methane ions in photoionization time-of-flight (TOF) mass spectra (Fig. S1) as the sole bimolecular reaction product. In the absence of other measurable spectral differences at an 8-fold higher precursor concentration, we can state that bimolecular chemistry was suppressed effectively, as also discussed in a previous study with the same reactor in similar conditions [43]. Consequently, hydrogen assisted fragmentations or bimolecular hydrogen abstraction reactions by fuel radicals only play a subordinate role. A molecular beam was formed at the exit of the microreactor, which was skimmed before entering the ionization chamber. The photoionization region is roughly 200 mm downstream from the reactor. There, the beam of tunable VUV photons crossed the molecular beam and yielded photoelectrons and photoions, which were extracted in opposite directions by a constant, 120 V•cm^{-1}, electric field. Photoelectrons were velocity map imaged and detected by a position-sensitive delay-line anode detector (Roentdek, DLD40) [30]. Threshold electrons with less than 3–5 meV kinetic energy were projected onto the central spot of detector, together with kinetic energy electrons without an off-axis momentum component. The hot electron contamination was subtracted using the signal intensity in a small ring around the center as proposed by Sztáray and Baer [29]. The photoions were space focused and detected by a microchannel plate detector and the electron signal was used as the start signal for the ion TOF analysis [30]. The ms-TPES of ion channels of interest were recorded by plotting the threshold photoelectron signal arriving in coincidence with an ion signal in the TOF window of the *m/z* of interest as a function of photon energy.

High-level *ab initio* calculations are necessary to rationalize the pyrolysis products and reveal the decomposition mechanism of $MeOCH_2OMe$, especially in the presence of isomerization pathways. Intermediates, transition states, and products in the thermal decomposition and/or the dissociative photoionization (DPI) processes of $MeOCH_2OMe$ were located on the ground state potential energy surface of neutrals and cations using density functional theory at the B3LYP/6-311++G(d,p) level. Intrinsic reaction coordinate (IRC) calculations [44,45] were carried out to validate that the located transition states indeed connect the assumed reactant and product(s). Based on the optimized geometries, the energies of these key species were calculated using the CBS-QB3 composite method [45], which has an average deviation of 4−5 kJ•mol^{-1} [45,46]. Quantum chemical calculations were performed using the Gaussian 16 A.03 program package [47]. Spin contamination was always small (< 10%) along the investigated open-shell reaction pathways and multireference effects, as addressed in literature MRCI calculations, also appear to be minor. Nevertheless, the energies of transition states and minima with significant strain could be somewhat less accurate.

To distinguish fragment ions, i.e., the products of $MeOCH_2OMe$ dissociative photoionization, from the parent peaks of the thermal decomposition products, the $MeOCH_2OMe$ breakdown diagram, i.e., the fractional ion abundances in the threshold photoionization of $MeOCH_2OMe$ as a function of photon energy, was plotted and analyzed. A statistical model for the DPI process was constructed to reproduce fractional ion abundances in the breakdown diagram as described in detail previously [48,49]. The Rice−Ramsperger−Kassel−Marcus (RRKM) statistical model [50–52] requires the densities and numbers of states of reactants and transition states, respectively, as well as the density of states of the neutral in order to obtain the internal energy distribution of the cation after threshold ionization. These were calculated using computed vibrational frequencies and rotational constants. The appearance energies, as well as the transitional frequencies were then varied so that the model reproduces the measured data.

3. Results and discussion

3.1. Dissociative photoionization of $MeOCH_2OMe$

$MeOCH_2OMe$ room temperature photoionization TOF-MS were measured in the 9.5–13.9 eV photon energy range. Figure 1(a) shows mass spectra at four representative energies: 10.21, 11.00, 12.00, and 13.87 eV, accepting all detected electrons as start signal. Two major fragment ions of *m/z* 75 ($C_3H_7O_2^+$) and 45 ($C_2H_5O^+$) were observed at low photon energies, and another fragment ion, *m/z* 47 ($C_2H_7O^+$), appeared beyond 12.6 eV with a small abundance. No parent ion ($C_3H_8O_2^+$, *m/z* 76) could be observed indicating that the parent ion is unstable in the Franck–Condon region. These results are generally consistent with the conclusions of the recent pre-shock experiment [18]. Threshold photoionization mass spectra are shown for comparison in Fig. 1(b). As the leaving electron does not remove energy from the system, the parent ion is more energetic, which is why threshold photoionization mass spectra exhibit a larger degree of fragmentation.

Below 10.5 eV, the predominant fragment ion of *m/z* 75 is the product of H loss from the $MeOCH_2OMe$ ion (76 amu). As shown in previous studies [31,33,34,40], slow ionic dissociation rate constants in the 10^3−10^7 s^{-1} range result in an asymmetric fragment ion peak shape in our PEPICO experiment. The *m/z* 75 peak showed a symmetric TOF profile with no shift as a function of energy. This is different from the similar H-loss from ethanol and furfural cations [41,53] and means that H loss from $MeOCH_2OMe$ is always faster than 10^7 s^{-1}, and, barring a large gap between the adiabatic ionization energy and the onset of the Franck–Condon envelope, i.e., the ion signal [54], it is indicative of easy C–H bond fission on the potential energy surface of parent ion in its electronic ground state. With the increase of photon energy, the *m/z* 75 intensity diminished, while the ion abundance of *m/z* 45 increased quickly and became dominant. Figure 2 shows the breakdown diagram for the major dissociation pathways based on the threshold ionization PEPICO TOF-MS in Fig. 1(b). Because $MeOCH_2OMe$ dissociatively photoionizes at the signal onset, the abundance of the H-loss fragment ion, $C_3H_7O_2^+$ (*m/z* 75), is 100% at the low-energy limit and the parent ion is not plotted in Fig. 2.

As shown in Fig. 2, $C_2H_5O^+$ (*m/z* 45) ions appear above 10.6 eV photon energy and the abundance of $C_3H_7O_2^+$ (*m/z* 75) drops. The $C_2H_5O^+$ abundance plateaus at ca. 90%, while 10% of the $C_3H_7O_2^+$ fragments persist in the breakdown diagram. Thus, either the $C_2H_5O^+$ (*m/z* 45) fragment ions are formed in a parallel process from the dissociation of parent ions, or two *m/z* 75 isomers are formed from the parent ion, one of which is stable with respect to formaldehyde (H_2CO, 30 amu) loss. Above 12.6 eV, the remaining *m/z* 75 fraction proceeds to yield $C_2H_7O^+$ ($CH_3O(H)CH_3^+$, *m/z* 47) fragment ion by CO loss.

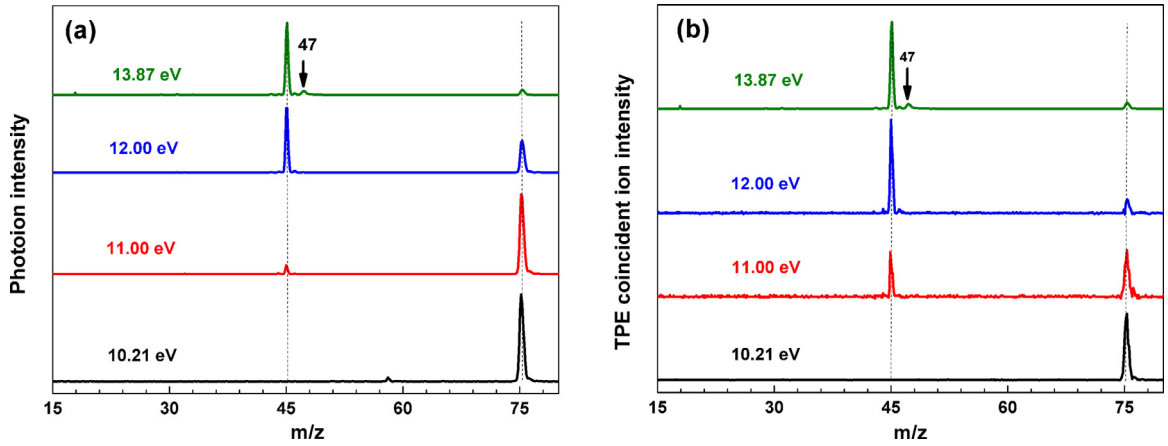

Fig. 1. All-electron photoionization (a) and threshold ionization PEPICO (b) TOF mass spectra of room temperature $MeOCH_2OMe$ at four representative photon energies, 10.21, 11.00, 12.00 and 13.87 eV.

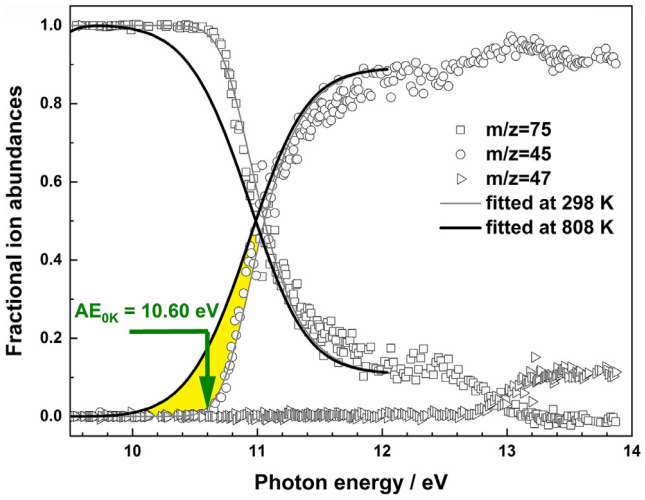

Fig. 2. Breakdown diagram of $MeOCH_2OMe$ ions, where hollow markers show the experimental fractional ion abundances, while the solid lines are the RRKM modeled curves to obtain the appearance energies. The appearance energy of $C_2H_5O^+$ (m/z 45) is determined as 10.60 ± 0.05 eV.

Our primary aim is to unveil the unimolecular decomposition of neutral $MeOCH_2OMe$. However, understanding the dissociative photoionization is crucial to distinguish between neutral decomposition products and the fragment ions of the parent $MeOCH_2OMe$ molecule. Herein, the optimized geometries of $MeOCH_2OMe^+$, $C_3H_7O_2^+$ (m/z 75) and $C_2H_5O^+$ (m/z 45) fragment ions, as well as the corresponding harmonic vibrational frequencies were calculated and a statistical model was fitted to reproduce the breakdown diagram at lower photon energies [48]. Based on this, the appearance energy for $C_2H_5O^+$ (m/z 45) is determined to be 10.60 ± 0.05 eV, which is consistent with the computed threshold, 10.84 eV at the CBS-QB3 level, for this most feasible $MeOCH_2OMe$ ion decomposition pathway (Fig. S2).

3.2. Photoionization TOF-MS in pyrolysis of $MeOCH_2OMe$

Since the ionization energies of most $MeOCH_2OMe$ pyrolysis products are below 11.0 eV, they can be detected at this photon energy: e.g., IE(CH_3, methyl, m/z 15) = 9.84 eV [34,40,55–57], IE(HCO, m/z 29) = 8.14 eV [58], IE(H_2CO, formaldehyde, m/z 30) = 10.88 eV [59], IE(HCOH, m/z 30) = 8.92 eV (calculated at the CBS-QB3 level), IE(CH_3O, methoxy, m/z 31) = 10.72 eV [60], IE(CH_2OH, hydroxymethyl, m/z 31) = 7.56 eV [60,61], IE(CH_3OH, methanol, m/z 32) = 10.84 eV [62], and IE(CH_3OCH_2, m/z 45) = 6.9 eV [63]. Figure 3 shows photoionization mass spectra recorded at several representative pyrolysis temperatures, indicative of a temperature-dependent product distribution. As discussed above, the $MeOCH_2OMe$ fragment ions $C_3H_7O_2^+$ (m/z 75) and $C_2H_5O^+$ (m/z 45) may be produced in dissociative photoionization at 11.00 eV.

When comparing with the room temperature data, the $C_2H_5O^+$ (m/z 45) peak becomes dominant at the expense of the m/z 75 peak at 1013 K. However, this is not due to efficient pyrolysis at 1013 K, but rather to the higher initial thermal energy of neutral $MeOCH_2OMe$, which also contributes to dissociative photoionization. The resulting redshift of the appearance energies increases the abundance of higher-onset fragment ions [15]. There are two ways to address the role of the precursor temperature on the mass spectra. First, and as shown in Fig. 3, the fractional ion abundance of m/z 45 increases significantly already at temperatures below the apparent pyrolysis onset, from 298 to 808 K. Second, we can rely on the statistical DPI model fitted to the room temperature data and increase the model temperature to 808 K. As seen in Fig. 2, the model predicts a much higher integral m/z 45 fractional abundance at 11 eV at a temperature of 808 K, compared with that at room temperature (see highlighted range in Fig. 2). Thus, the m/z 45 and 75 peaks are fully attributed to DPI of $MeOCH_2OMe$.

When the pyrolysis temperature was raised to 1013 K, new peaks appeared at m/z 15, 29, 30, 31, and 32. They can tentatively be assigned to CH_3^+, HCO^+, H_2CO^+(or $HCOH^+$), CH_3O^+ (or CH_2OH^+), and CH_3OH^+, respectively. As these peaks are absent in the DPI measurements of $MeOCH_2OMe$, they are the result of thermal decomposition of neutral $MeOCH_2OMe$ molecules. When the temperature was increased to 1143 K, the light decomposition products (m/z < 45) became more dominant, while almost all the m/z 75 fragments disappeared and only a small amount of m/z 45 survived. The phenomenon was more pronounced at 1243 K, at which temperature methyl radicals were dominant, while the m/z 45 fragment ion completely disappeared, indicating quantitative thermal decomposition of $MeOCH_2OMe$ in the reactor. We also recorded mass spectra and ms-TPES at pyrolysis temperatures of 1143 and 1243 K at 14 eV photon energy to detect CO at m/z 28 and the CH_4 at m/z 16 (Figs. S3–S5 in Supplementary Information). This hints at sequential dissociation steps of the primary pyrolysis products of $MeOCH_2OMe$ as also seen in the temperature-dependent behavior in Fig. 3.

3.3. Identification of the m/z 30 and 31 fragments, quantification of molecular beam cooling

As mentioned above, there are multiple possible m/z 30 and 31 isomers among the $MeOCH_2OMe$ pyrolysis products. Previous stud-

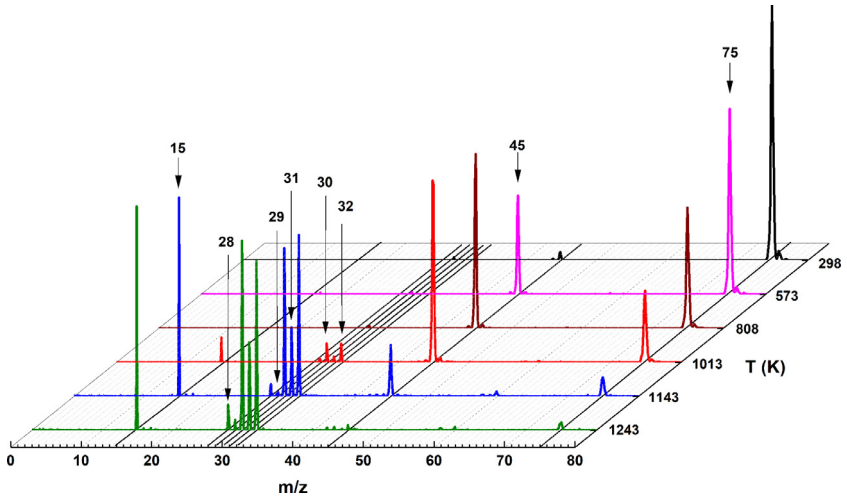

Fig. 3. Photoionization TOF mass spectra of $MeOCH_2OMe$ with pyrolysis at several representative temperatures measured at 11.0 eV photon energy.

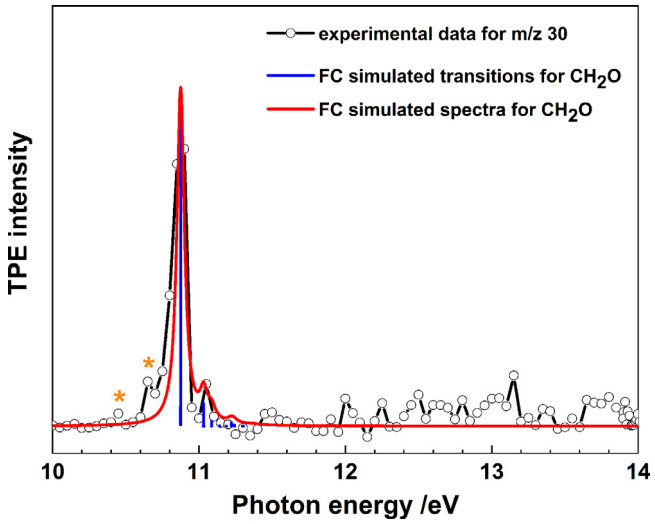

Fig. 4. Photoion mass-selected threshold photoelectron spectrum of the *m/z* 30 fragment.

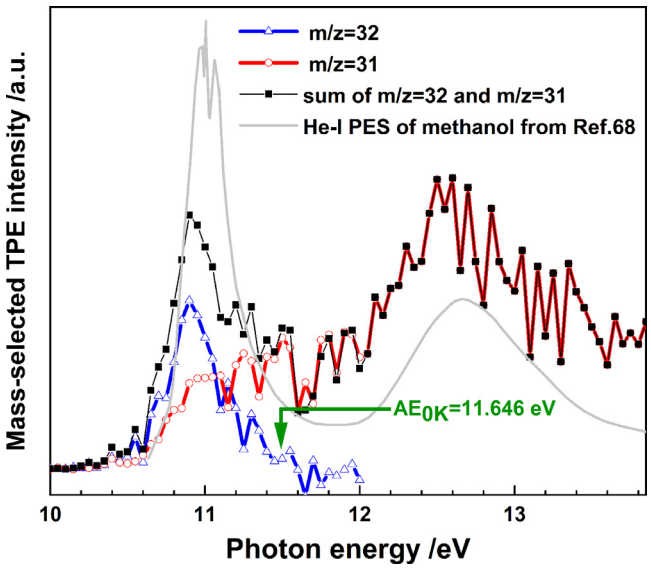

Fig. 5. Photoion mass-selected threshold photoelectron spectra of the *m/z* 31 and 32 signals, where the black trace is the sum of the *m/z* 31 and 32 signals, and the gray solid line is the reported He-I photoelectron spectrum of methanol from Ref. [68].

ies show that ms-TPES is a sensitive, selective and universal detection tool to discern isomers when, as is often the case, ionization energies or vibrational progressions are different enough [32,64].

The ms-TPES for the *m/z* 30 fragment was recorded at 1243 K with a step size of 50 meV (Fig. 4). A single band with small shoulders was observed with no clearly discerned vibrational structure indicating vertical ionization and a strong origin peak. The measured ionization energy of 10.90 eV is consistent with the adiabatic ionization energy of formaldehyde, 10.88 eV [65]. The small peaks at 10.65 and 10.45 eV (noted with stars) are attributed to hot and sequence band transitions. Hydroxymethylene carbene, HCOH, which is 2.30 eV (CBS-QB3) less stable than formaldehyde, is not observed, as the calculated ionization energy of 8.92 eV, far below the observed signal onset. Thus, this fragment of *m/z* 30 is assigned to the formaldehyde (H_2CO) pyrolysis product.

We have considered CH_3O (methoxy radical) and CH_2OH (hydroxymethyl radical) as carriers of the *m/z* 31 peak. Figure 5 shows the recorded ms-TPES for the *m/z* 31 fragment, which exhibits a broad profile in the 10.5–14.0 eV range, similar to the *m/z* 32 signal. However, as no *m/z* 31 signal was observed below 10 eV, the hydroxymethyl radical (IE_a = 7.56 eV [60,61]) does not contribute to the spectrum. Although, the reported methoxy radical IE_a is 10.72 eV [60] and, thus, close to the band onset, our theoretical calculations in Section 3.4 question whether methoxy radicals contribute to the spectrum, because the activation energy to methoxy radical formation in $MeOCH_2OMe$ pyrolysis is too high. More importantly, the spectrum in Fig. 5 deviates strongly from the TPES of the methoxy radical (Fig. S6) [66]. Thus, the *m/z* 31 signal is most likely due to dissociative photoionization of a heavier pyrolysis product. According to literature results [25,67], *m/z* 31 ions are readily produced in the DPI of room temperature methanol above a photon energy of 11.5 eV. “Hot” methanol, as a feasible pyrolysis product of $MeOCH_2OMe$, will dissociatively ionize at lower photon energies, a phenomenon also seen in the decomposition of phosphororganic compounds [25]. In fact, the sum of the *m/z* 31 and 32 ms-TPE signals is in good agreement with the expected methanol TPES (Fig. 5), as compared with the reported He-I photoelectron spectrum [68] with a slight thermal redshift. Furthermore, the fractional abundance of these two peaks can be plotted in a breakdown diagram, to be modeled using the methanol DPI model of Borkar et al. [67] (Fig. S7). This allows us to determine a

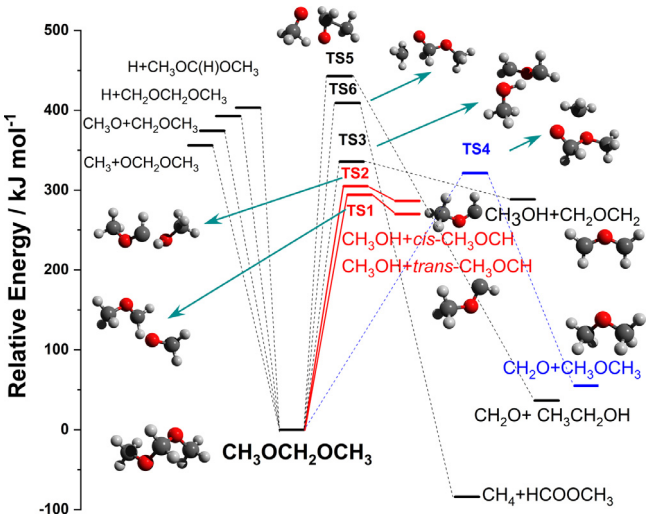

Fig. 6. Computed primary initial fragmentation pathways of $MeOCH_2OMe$, relative to neutral $MeOCH_2OMe$ molecule, at the CBS-QB3 level. The red solid lines show the most feasible pathways, and the blue line corresponds to the secondary one, while black dashed lines show minor channels.

Table 1
Relative energies of the transition states and products involved in the primary decomposition pathways of $MeOCH_2OMe$, calculated at the CBS-QB3 level.

Species	Relative energy ($kJ{\cdot}mol^{-1}$)	Description
$MeOCH_2OMe$	0	
$H+CH_2OCH_2OCH_3$	393	**(1)** C–H bond fission at methyl
$H+CH_3OC(H)OCH_3$	403	**(2)** C–H bond fission at methylene
$CH_3+OCH_2OCH_3$	356	**(3)** C–O bond fission
$CH_3O+CH_2OCH_3$	374	**(4)** C–O bond fission
CH_3OH+*trans*-CH_3OCH	270	**(5)** Methanol formation
TS1	294	
CH_3OH+*cis*-CH_3OCH	287	**(6)** Methanol formation
TS2	305	
$CH_3OH + CH_2OCH_2$	288	**(7)** Methanol formation
TS3	336	
$CH_2O+CH_3OCH_3$	55	**(8)** Formaldehyde formation by CH_3 migration
TS4	321	
$CH_2O+ CH_3CH_2OH$	37	**(9)** Formaldehyde formation by CH_3 and H migration
TS5	443	
$CH_4+ HCOOCH_3$	–84	**(10)** Methane formation
TS6	409	

phenomenological temperature for the pyrolysis product methanol [69]. Compared with the reactor temperature of 1243 K, the fitted temperature was found to be 850 K. The difference is due to collisional cooling in the molecular beam expansion from the pyrolysis microreactor, which was previously reported to be imperfect yet substantial [36].

3.4. *$MeOCH_2OMe$ potential energy surface*

Exploring the potential energy surface of $MeOCH_2OMe$ is necessary to understand the decomposition pathways, to unravel the dissociation mechanism and to explain the temperature-dependent changes of the branching ratios. Composite quantum chemical calculations were guided by experimental observations. The major pyrolysis products are CH_3, CO, HCO, H_2CO (formaldehyde), CH_3OH, CH_3OCH_2, and $C_3H_7O_2$, which can be classified as primary products and the products of sequential decomposition channels.

Figure 6 shows the primary fragmentation pathways of neutral $MeOCH_2OMe$. As the $MeOCH_2OMe$ conformational isomers are almost isoenergetic ($\Delta E < 11$ $kJ{\cdot}mol^{-1}$ at the CBS-QB3 level) and the barriers among them are also low (ca. 30 $kJ{\cdot}mol^{-1}$), due to barely hindered internal rotation around the C–O bond, we only show the most stable conformer in Fig. 6. The relative energies of the transition states and heats of reaction for the primary decomposition at the CBS-QB3 level are summarized in Table 1.

H-loss from the methyl and methylene groups of $MeOCH_2OMe$ are strongly endothermic by 393 and 403 $kJ{\cdot}mol^{-1}$ (see (1–2) in Table 1), respectively. Such high bond energies confirm that C–H bond breaking only takes place in the cation and the *m/z* 75 ion signal is the result of dissociative photoionization of $MeOCH_2OMe$. Homolytic C–O bond fission in $MeOCH_2OMe$ may produce two pairs of free radicals, CH_3OCH_2O (*m/z* 61) and CH_3 (*m/z* 15) in methyl-loss, CH_3OCH_2 (*m/z* 45) and CH_3O (*m/z* 31) in methoxy-loss. The barrier heights are calculated at 356 and 374 $kJ{\cdot}mol^{-1}$, respectively (see (3–4) in Table 1). These bond energies are broadly consistent with the previous results [14–18], indicative of the comparable accuracy of the computational methods used.

In addition to these simple bond-breaking reactions, more complex pathways involving isomerization steps are proposed to play a role in $MeOCH_2OMe$ thermal decomposition. Three feasible mechanisms yield CH_3OH: (5)–(7). The first two pathways proceed via H migration from the methylene group to the adjacent oxygen atom, followed by C–O bond fission. Methanol (CH_3OH, *m/z* 32) and methoxymethylene carbene, CH_3OCH (*m/z* 44), are formed as products. The corresponding barriers are 294 and 305 $kJ{\cdot}mol^{-1}$ to produce *trans*- and *cis*-CH_3OCH (Fig. 6), and the pathways are endothermic by 270 and 287 $kJ{\cdot}mol^{-1}$, respectively. H migration from one of the methyl groups to the more distant oxygen atom can also lead to a methanol-loss when followed by C–O bond breaking, accompanied by the formation of the CH_2OCH_2 (*m/z* 44) diradical. The overall process is endothermic by 288 $kJ{\cdot}mol^{-1}$ and has to pass a higher barrier of 336 $kJ{\cdot}mol^{-1}$ (7). As shown in Table 1 and Fig. 6, the direct CH_3OH-loss pathways are much more favorable in energy than C–H or C–O bond fission, which suggests that they may be included in future $MeOCH_2OMe$ kinetic models [14–18].

Besides methanol, formaldehyde can also be formed directly in the thermal decomposition of $MeOCH_2OMe$ along two pathways as shown in Fig. 6, (8–9). The lower-lying path proceeds by methyl migration to the more distant oxygen atom, associated with C–O bond fission, to yield dimethyl ether (CH_3OCH_3, *m/z* 46) and formaldehyde (H_2CO, *m/z* 30) with a barrier of 321 $kJ{\cdot}mol^{-1}$. The more energetic pathway yields formaldehyde and ethanol, but is unlikely to occur due to its high barrier (TS5, 443 $kJ{\cdot}mol^{-1}$), even higher than the direct bond breaking energies, which, in contrast to isomerization reactions, proceed over loose transition states (9). In addition, methane can be produced directly via TS6, in (10). During the reaction, H migration takes place from the methylene group to one of the methyl groups, followed immediately by C–O bond breaking and the release of methane and methyl formate. Although the overall process is exothermic, methane formation is unlikely because of the tight and high-energy transition state at 409 $kJ{\cdot}mol^{-1}$.

Thus, the dissociation reactions (5) and (6) to produce the methoxycarbene CH_3OCH and methanol primary fragments are most likely dominant because of their favored energetics among the initial decomposition pathways. Furthermore, dimethyl ether and formaldehyde can also be produced at a slightly higher barrier. Because of the excess energy redistribution, smaller in methanol but significant in formaldehyde formation, the effective temperatures of these products are expected to be elevated from the start. Furthermore, they are expected to be re-thermalized during the 10–100 μs long contact time in the microreactor [70]. Thus, their further, sequential dissociation processes also have to be considered.

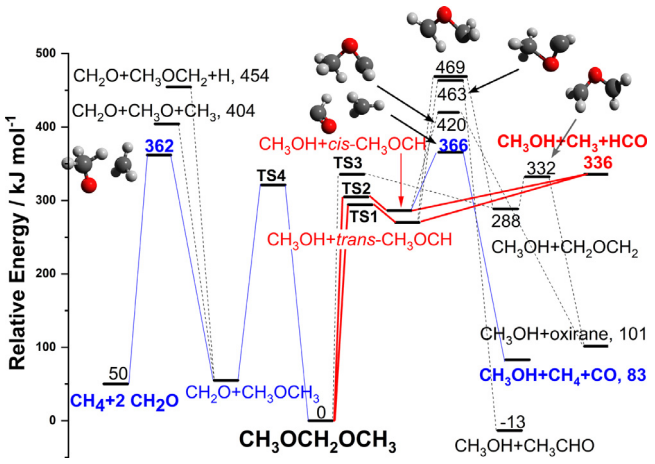

Fig. 7. Further decomposition pathways of the dominant primary fragments in pyrolysis of $MeOCH_2OMe$, where the relative energies to neutral $MeOCH_2OMe$ molecule are calculated at the CBS-QB3 level.

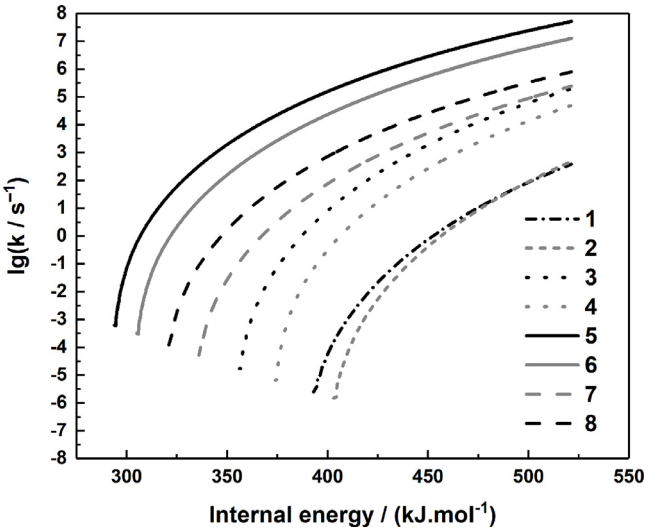

Fig. 8. RRKM unimolecular dissociation rate constants for each product pathway as function of $MeOCH_2OMe$ internal energy. Solid lines refer to the isomerization–decomposition channels and dashed lines indicate direct bond fission processes.

Figure 7 shows the computed sequential decomposition pathways from the primary fragments, namely the CH_3OCH and dimethyl ether. As shown in Fig. 7, both *trans*- and *cis*-CH_3OCH can dissociate further at small excess energies to the more stable fragments, HCO (*m/z* 29) and methyl (*m/z* 15) radical. The simple C–O bond fission is only slightly endothermic by 66 kJ•mol^{-1} in *trans*-CH_3OCH, and 49 kJ•mol^{-1} in *cis*-CH_3OCH, respectively. The small barrier and the expected fast re-thermalization in the microreactor explain the missing *m/z* 44 signal in the mass spectrum. Then, HCO easily dissociates to CO + H by overcoming a barrier of 73 kJ•mol^{-1}. The observed *m/z* 29 signal in the Fig. 3 is probably due to dissociative ionization of formaldehyde, which occurs already at 11 eV due to rovibrational excitation of CH_2O. In addition, there are two more stable isomers of CH_3OCH (*m/z* 44), namely acetaldehyde (CH_3CHO) and oxirane (*o*-CH_2OCH_2). As indicated in Fig. 7, for *trans*-CH_3OCH, the isomerization barriers to form acetaldehyde or the CH_2OCH_2 diradical (then isomerize to oxirane) are about 195 kJ•mol^{-1}, much higher than the barrier to decomposition to CH_3+HCO, which suggests that these more stable C_2H_4O isomers are not formed from *trans*-CH_3OCH. Moreover, since the *cis–trans* isomerization barrier is relatively high (108 kJ•mol^{-1} at CBS-QB3) in CH_3OCH (*m/z* 44), *cis*-CH_3OCH shows different decomposition pathways from *trans*-CH_3OCH except for the simple C–O fission, as shown in Fig. 7. The CH_4 + CO decomposition of *cis*-CH_3OCH has a lower barrier (79 kJ•mol^{-1}), while the oxirane can be formed via a moderately high barrier (133 kJ•mol^{-1}).

Dimethyl ether, another primary pyrolysis product with a minor abundance, is also expected to decompose further [71–74]. Direct C–O bond breaking needs at least 350 kJ•mol^{-1} to yield methoxy and methyl radicals, while the H-loss is even more endothermic by 400 kJ•mol^{-1}. However, methane can be produced after H migration at a lower barrier of 308 kJ•mol^{-1}, associated with the release of formaldehyde. In summary, methanol and CH_3OCH, formaldehyde and dimethyl ether, are expected to be initially formed in the pyrolysis process of $MeOCH_2OMe$, of which dimethyl ether and CH_3OCH is only an intermediate as they are comparably or significantly less thermally stable than $MeOCH_2OMe$. With the increase of reactor temperature, further sequential fragments, such as methyl (*m/z* 15), HCO radical (*m/z* 29), methane (*m/z* 16) and carbon monoxide (*m/z* 28), are produced. The structures of all the reactants, products and transitions states are summarized in Table S3.

3.5. Branching ratios of various decomposition products of $MeOCH_2OMe$

Based on the calculated potential energy surface of $MeOCH_2OMe$ decomposition, RRKM theory was employed to estimate unimolecular branching ratios over the various products [48,75]. For the direct bond breaking processes of (1–4), for which no saddle point was found, the transition state vibrational frequencies were approximated by frequency analysis at a constrained 3.5 Å bond length along the reaction coordinate. Figure 8 plots the calculated microcanonical rate constants for pathways (1–8) as the function of internal energy. At $MeOCH_2OMe$ internal energy of 450 kJ mol^{-1}, the main branching ratios are determined as 82.7% for (5), and 16.2% for (6). As shown in Table S1, the predicted contributions of other channels are negligible.

3.6. Pyrolysis mechanism of $MeOCH_2OMe$

Based on the temperature-dependent mass spectra and the calculated decomposition pathways, we can reveal the unimolecular decomposition mechanism of $MeOCH_2OMe$. Below about 923 K, $MeOCH_2OMe$ is stable at our reactor conditions and only the dissociative photoionization signals of $C_2H_5O^+$ (*m/z* 45) and $C_3H_7O^+$ (*m/z* 75) were observed in the mass spectra. When the reactor temperature was increased to 1013 K, the first decomposition products appeared at *m/z* 15, 30 and 32, indicative of the pyrolysis onset. As confirmed by our calculations, the primary decomposition of $MeOCH_2OMe$ proceeds via H-migration isomerization processes (TS1–TS4) followed by bond fissions to yield methanol and *trans*- (or *cis*-) CH_3OCH carbene, together with formaldehyde and dimethyl ether. In contrast to these complex primary fragmentation pathways, direct bond fission processes in $MeOCH_2OMe$ by H loss, or to produce CH_3OCH_2 and methoxy or methyl and CH_3OCH_2O, exhibit much higher activation energies and are not likely to take place. In previous $MeOCH_2OMe$ kinetic models, radicals produced by the primary unimolecular decomposition of fuel are critical to ignition processes [27], as H-abstraction together with the β-direct dissociations [76] were thought to play a trigger role and compete with the bimolecular reactions, such as oxidation. However, according to our results uni-

molecular isomerization–decomposition pathways may be equally important, especially at low pressure conditions.

Only trace amounts of CH_3OCH (*m/z* 44) and dimethyl either (*m/z* 46) are observed in Fig. 3, although their ionization energies are below 11 eV. The 10–100 μs residence time in the microreactor allows for re-thermalization, and thus, almost quantitative destruction of these primary pyrolysis products proceeds with further dissociation. The high dilution of the sample also means that recombination of the primary fragments and bimolecular chemistry in general is suppressed even in the absence of an entrance barrier for these processes.

As shown in Fig. 7, methyl and HCO radicals (*m/z* 15 and 29, respectively) are readily produced from CH_3OCH. There is a further, minor CH_3OCH fragmentation pathway yielding methane and carbon monoxide. Owing to the higher ionization energies of methane (IE_a = 12.61 eV) and carbon monoxide (IE_a = 14.01 eV), these products are not detected in the mass spectra in Fig. 3, but they were clearly observed in Figs. S3 and S4 when the photon energy was increased above their IE. Furthermore, as the major pyrolysis product, methanol (*m/z* 32) can dissociatively ionize to yield CH_2OH^+ (*m/z* 31) by H loss. Actually, the relative intensities of *m/z* 31 and 32 are well reproduced with the methanol DPI model [67].

With the increase of the reactor temperature, the relative abundance of the small fragments such as *m/z* 15, 30, 31 and 32 increased markedly, as shown in Fig. 3. As discussed above, the methyl radical (*m/z* 15) is produced by further decomposition of the primary fragments, *trans*- (or *cis*-) CH_3OCH. Naturally, the branching ratio of methyl radical is promoted with temperature due to the more efficient sequential dissociation. Furthermore, the intensity of the formaldehyde signal at *m/z* 30 overtook that of methanol at *m/z* 32 when the reactor temperature was increased. Based on the calculations in Figs. 6 and 7, formaldehyde can directly be yielded from pyrolysis of $MeOCH_2OMe$ over TS4, and moreover the sequential dissociation of methyl ether can also further produce formaldehyde by H-migration. Therefore, these two formation pathways of formaldehyde are consistent with the experiment. In summary, our calculations and experimental conclusions of the predominant products, e.g. *m/z* 15, 16, 28, 29, 30, 31 and 32, agree very well to propose the overall pyrolysis pathways of $MeOCH_2OMe$.

4. Conclusions

Pyrolysis of $MeOCH_2OMe$ has been investigated experimentally using *i*PEPICO with VUV synchrotron photoionization in the temperature range of 298 to 1243 K. The most stable products and some radical intermediates produced in pyrolysis of $MeOCH_2OMe$ were observed, e.g. *m/z* 15, 28, 29, 30, 31, 32, 45 and 75, and their temperature dependence was analyzed.

The photoionization mass spectra of $MeOCH_2OMe$ with and without pyrolysis confirm that the observed *m/z* 45 and 75 ions originate from dissociative ionization (DPI) of $MeOCH_2OMe$. Cursory analysis of the $MeOCH_2OMe$ breakdown diagram revealed the 0 K appearance energy for $C_2H_5O^+$ (*m/z* 45) as AE_0 = 10.60 ± 0.05 eV. The other peaks, which arise at temperatures greater than 923 K, are due to primary and secondary unimolecular thermal decomposition pathways of neutral $MeOCH_2OMe$, as well as the dissociative photoionization of the main primary products, methanol and formaldehyde. The ms-TPES are used to identify the isomers for each pyrolysis fragment. It is noted that the *m/z* 31 signal was attributed to the methoxy radical in the previous studies [16,17] but our spectral analysis clearly shows that this is due to the hydroxymethyl ions produced in the DPI of methanol [15–19].

Based on the theoretical calculations at the CBS-QB3 level of theory, new insights were gained in the decomposition mechanism of $MeOCH_2OMe$. The primary H-migration channel to yield hydroxymethylene (CH_3OCH) and methanol is the thermodynamically most favored one, while methyl ether and formaldehyde are readily produced too. On the contrary, the C-H and C–O bond fissions in $MeOCH_2OMe$, which were previously proposed to be the primary initial steps of $MeOCH_2OMe$ pyrolysis reactions, are high in energy and unlikely to compete with the isomerization reactions. Calculations have also revealed that the sequential dissociation of CH_3OCH and dimethyl ether at high temperature can contribute to the enhanced *m/z* 15, 28 and 29 signals [71–74]. Therefore, our investigation not only proposes a thermal decomposition mechanism of $MeOCH_2OMe$ itself, but also provides some new mechanistic clues to be considered in kinetic models.

Declaration of Competing Interest

There are no conflicts of interest to declare.

Acknowledgments

The financial support of the Swiss Federal Office for Energy (BFE Contract No. SI/501269-01) and the National Natural Science Foundation of China (Nos. 21573210, 21903079 and 21873089) are gratefully acknowledged. The work is also financially supported by the National Key Research and Development Program of China (No. 2016YFF0200502), the Chinese Postdoctoral Foundation (No. 2018M632535) and the USTC-NSRL Association. X. Wu also thanks the SSSTC scholarship (No. EG-CN 01-042018) and China Scholarship Council (No. 201806340001) for support. X. Zhou appreciates Dr. Xiaofeng Tang for sending us the unpublished ms-TPES data of methoxy radical for comparison. The authors thank the referees for their insights into the methylal kinetics.

Supplementary materials

Supplementary material associated with this article can be found, in the online version, at doi:10.1016/j.combustflame.2020.08.040.

References

[1] J. Abboud, J. Schobing, G. Legros, J. Bonnety, V. Tschamber, A. Brillard, G. Leyssens, V. Lauga, E.E. Iojoiu, P. Da Costa, Impacts of oxygenated compounds concentration on sooting propensities and soot oxidative reactivity: application to diesel and biodiesel surrogates, Fuel 193 (2017) 241–253.
[2] L. Coniglio, H. Bennadji, P.A. Glaude, O. Herbinet, F. Billaud, Combustion chemical kinetics of biodiesel and related compounds (methyl and ethyl esters): experiments and modeling – advances and future refinements, Prog. Energy Combust. Sci. 39 (2017) 340–382.
[3] E. Khalife, M. Tabatabaei, A. Demirbas, M. Aghbashlo, Impacts of additives on performance and emission characteristics of diesel engines during steady state operation, Prog. Energy Combust. Sci. 59 (2017) 32–78.
[4] K. Kohse-Höinghaus, P. Oßwald, T.A. Cool, T. Kasper, N. Hansen, F. Qi, C.K. Westbrook, P.R. Westmoreland, Biofuel combustion chemistry: from ethanol to biodiesel, Angew. Chem. Int. Ed. 49 (2010) 3572–3597.
[5] A.K. Agarwal, Biofuels (alcohols and biodiesel) applications as fuels for internal combustion engines, Prog. Energy Combust. Sci. 33 (2007) 233–271.
[6] N.M. Ribeiro, A.C. Pinto, C.M. Quintella, G.O. da Rocha, L.S.G. Teixeira, L.L.N. Guarieiro, M. do Carmo, Rangel, M.C.C. Veloso, M.J.C. Rezende, R. Serpa da Cruz, A.M. de Oliveira, E.A. Torres, J.B. de Andrade, The role of additives for diesel and diesel blended (ethanol or biodiesel) fuels: a review, Energy Fuels 21 (2007) 2433–2445.
[7] J. Burger, M. Siegert, E. Stroefer, H. Hasse, Poly(oxymethylene) dimethyl ethers as components of tailored diesel fuel: properties, synthesis and purification concepts, Fuel 89 (2010) 3315–3319.
[8] J. Burger, H. Hasse, Multi-objective optimization using reduced models in conceptual design of a fuel additive production process, Chem. Eng. Sci. 99 (2013) 118–126.
[9] H. Liu, Z. Wang, J. Wang, X. He, Improvement of emission characteristics and thermal efficiency in diesel engines by fueling gasoline/diesel/PODEn blends, Energy 97 (2016) 105–112.
[10] Y. Ren, Z.H. Huang, H.Y. Miao, Y. Di, D. Jiang, K. Zeng, B. Liu, X. Wang, Combustion and emissions of a DI diesel engine fuelled with diesel-oxygenate blends, Fuel 87 (2008) 2691–2697.

[11] J. Yan, T. Shamim, S. Chou, H. Li, Z. Wang, H. Liu, J. Zhang, J. Wang, S. Shuai, Clean efficient and affordable energy for a sustainable future: the 7th international conference on applied energy (ICAE2015) performance, combustion and emission characteristics of a diesel engine fueled with polyoxymethylene dimethyl ethers (PODE3-4)/diesel blends, Energy Proc. 75 (2015) 2337–2344.

[12] M.B. Sirman, E.C. Owens, K.A. Whitney, Emissions comparison of alternative fuels in an advanced automotive diesel engine, Southwest Research Institute, 1998 Report for DOE and U.S. Army TARDEC.

[13] K.D. Vertin, J.M. Ohi, D.W. Naegeli, K.H. Childress, G.P. Hagen, C.I. McCarthy, A.S. Cheng, R.W. Dibble. Methylal and methylal-diesel-blended fuels for use in compression-ignition engines. SAE Technical Paper. 1999, Series no 1999-01-1508.

[14] W.A. Kopp, L.C. Kröger, M. Döntgen, S. Jacobs, U. Burke, H.J. Curran, K. Alexander Heufer, K. Leonhard, Detailed kinetic modeling of dimethoxymethane. Part I: ab initio thermochemistry and kinetics predictions for key reactions, Combust. Flame 189 (2018) 433–442.

[15] F.H. Vermeire, H.H. Carstensen, O. Herbinet, F. Battin-Leclerc, G.B. Marin, K.M. Van Geem, Experimental and modeling study of the pyrolysis and combustion of dimethoxymethane, Combust. Flame 190 (2018) 270–283.

[16] W.Y. Sun, T. Tao, M. Lailliau, N. Hansen, B. Yang, P. Dagaut, Exploration of the oxidation chemistry of dimeth-oxymethane: jet-stirred reactor experiments and kinetic modeling, Combust. Flame 193 (2018) 491–501.

[17] S. Peukert, P. Sela, D. Nativel, J. Herzler, M. Fikri, C. Schulz, Direct measurement of high-temperature rate constants of the thermal decomposition of dimethoxymethane, a shock tube and modeling study, J. Phys. Chem. A 122 (2018) 7559–7571.

[18] L. Golka, I. Weber, M. Olzmann, Pyrolysis of dimethoxymethane and the reaction of dimethoxymethane with H atoms: a shock-tube/ARAS/TOF-MS and modeling study, Proc. Combust. Inst. 37 (2019) 179–187.

[19] L. Marrodán, E. Royo, Á. Millera, R. Bilbao, M.U. Alzueta, High pressure oxidation of dimethoxymethane, Energy Fuels 29 (2015) 3507–3517.

[20] L. Golka, D. Gratzfeld, I. Weber, M. Olzmann, Temperature- and pressure-dependent kinetics of the competing C–O bond fission reactions of dimethoxymethane, Phys. Chem. Chem. Phys. 22 (2020) 5523–5530.

[21] T.J. He, Z. Wang, X.Q. You, H.Y. Liu, Y.D. Wang, X.Y. Li, X. He, A chemical kinetic mechanism for the low- and intermediate-temperature combustion of Polyoxymethylene Dimethyl Ether 3 ($PODE_3$), Fuel 212 (2018) 223–235.

[22] S. Jacobs, M. Döntgen, A.B.S. Alquaity, W.A. Kopp, L. Kröger, U. Burke, H. Pitsch, K. Leonhard, H. Curran, K.A. Heufer, Detailed kinetic modeling of dimethoxymethane. Part II: experimental and theoretical study of the kinetics and reaction mechanism, Combust. Flame 205 (2019) 522–533.

[23] E.j. Hu, Z.H. Gao, Y. Liu, G.Y. Yin, Z.H. Huang, Experimental and modeling study on ignition delay times of dimethoxy methane/n-heptane blends, Fuel 189 (2017) 350–357.

[24] D. Krüger, P. Oßwald, M. Köhler, P. Hemberger, T. Bierkandt, Y. Karakaya, T. Kasper, Hydrogen abstraction ratios: a systematic iPEPICO spectroscopic investigation in laminar flames, Combust. Flame 191 (2018) 343–352.

[25] S.Y. Liang, P. Hemberger, N.M. Neisius, A. Bodi, H. Grutzmacher, J. Levalois–Grutzmacher, S. Gaan, Elucidating the thermal decomposition of dimethyl methylphosphonate by vacuum ultraviolet (VUV) photoionization: pathways to the PO radical, a key species in flame-retardant mechanisms, Chem. – Eur. J. 21 (2015) 1073–1080.

[26] M. Gerlach, A. Bodi, P. Hemberger, Metamorphic meta isomer: carbon dioxide and ketenes are formed via retro-Diels-Alder reactions in the decomposition of meta-benzenediol, Phys. Chem. Chem. Phys. 21 (2019) 19480–19487.

[27] J.I.M. Pastoors, A. Bodi, P. Hemberger, J. Bouwman, Dissociative ionization and thermal decomposition of cyclopentanone, Chemistry 23 (2017) 13131–13140.

[28] X.K. Wu, X.F. Tang, X.G. Zhou, S.L. Liu, Dissociation dynamics of energy-selected ions with threshold photoelectron-photoion coincidence velocity imaging, Chin. J. Chem. Phys. 31 (2019) 11–32.

[29] B. Sztáray, T. Baer, Suppression of hot electrons in threshold photoelectron photoion coincidence spectroscopy using velocity focusing optics, Rev. Sci. Instrum. 74 (2003) 3763–3768.

[30] K. Voronova, C.M. Mozaffari Easter, K.J. Covert, A. Bodi, P. Hemberger, B. Sztáray, Dissociative photoionization of diethyl ether, J. Phys. Chem. A 119 (2015) 10654–10663.

[31] G. Muller, K. Voronova, B. Sztáray, G. Meloni, Rotamers and migration: investigating the dissociative photoionization of ethylenediamine, J. Phys. Chem. A 120 (2016) 3906–3916.

[32] J. Bouwman, B. Sztáray, J. Oomens, P. Hemberger, A. Bodi, Dissociative photoionization of quinoline and isoquinoline, J. Phys. Chem. A 119 (2015) 1127–1136.

[33] P. Hemberger, G. da Silva, A.J. Trevitt, T. Gerber, A. Bodi, Are the three hydroxyphenyl radical isomers created equal? – The role of the phenoxy radical, Phys. Chem. Chem. Phys. 17 (2015) 30076–30083.

[34] P. Hemberger, A.J. Trevitt, T. Gerber, E. Ross, G. da Silva, Isomer-specific product detection of gas-phase xylyl radical rearrangement and decomposition using VUV synchrotron photoionization, J. Phys. Chem. A 118 (2014) 3593–3604.

[35] P. Hemberger, A.J. Trevitt, T. Gerber, E. Ross, G. da Silva, Direct observation of para-Xylylene as the decomposition product of the meta-Xylyl radical using VUV synchrotron radiation, J. Phys. Chem. Lett. 4 (2013) 2546–2550.

[36] B.K.C. de Miranda, C. Alcaraz, M. Elhanine, B. Noller, P. Hemberger, I. Fischer, G.A. Garcia, H. Soldi-Lose, B. Gans, L.A.V. Mendes, S. Boye-Peronne, S. Douin, J. Zabka, P. Botschwina, Threshold photoelectron spectroscopy of the methyl radical isotopomers, CH_3, CH_2D, CHD_2 and CD_3: synergy between VUV synchrotron radiation experiments and explicitly correlated coupled cluster calculations, J. Phys. Chem. A 114 (2010) 4818–4830.

[37] M. Winfough, K. Voronova, G. Muller, G. Laguisma, B. Sztaray, A. Bodi, G. Meloni, Furfural: the unimolecular dissociative photoionization mechanism of the simplest furanic aldehyde, J. Phys. Chem. A 121 (2017) 3401–3410.

[38] A. Bodi, P. Hemberger, D.L. Osborn, B. Sztáray, Mass-resolved isomer-selective chemical analysis with imaging photoelectron photoion coincidence spectroscopy, J. Phys. Chem. Lett. 4 (2013) 2948–2952.

[39] M. Johnson, A. Bodi, L. Schulz, T. Gerber, Vacuum ultraviolet beamline at the swiss light source for chemical dynamics studies, Nucl. Instrum. Methods Phys. Res. Sect. A 610 (2009) 597–603.

[40] A. Bodi, B. Sztáray, T. Baer, M. Johnson, T. Gerber, Data acquisition schemes for continuous two-particle time-of-flight coincidence experiments, Rev. Sci. Instrum. 78 (2007) 084102.

[41] A. Bodi, M. Johnson, T. Gerber, Z. Gengeliczki, B. Sztáray, T. Baer, Imaging photoelectron photoion coincidence spectroscopy with velocity focusing electron optics, Rev. Sci. Instrum, 80 (2009) 034101.

[42] D.W. Kohn, H. Clauberg, P. Chen, Flash pyrolysis nozzle for generation of radicals in a supersonic jet expansion, Rev. Sci. Instrum. 63 (1992) 4003–4005.

[43] A.K. Vasiliou, J.H. Kim, T.K. Ormond, K.M. Piech, K.N. Urness, A.M. Scheer, D.J. Robichaud, C. Mukarakate, M.R. Nimlos, J.W. Daily, Q. Guan, H.H. Carstensen, G.B. Ellison, Biomass pyrolysis: thermal decomposition mechanisms of furfural and benzaldehyde, J. Chem. Phys. 139 (2013) 104310.

[44] C. Lee, W.T. Yang, R.G. Parr, Development of the Colle-Salvetti correlation-energy formula into a functional of the electron density, Phys. Rev. B 37 (1988) 785–789.

[45] J.A. Montgomery, M.J. Frisch, J.W. Ochterski, G.A. Petersson, A complete basis set model chemistry. VI. Use of density functional geometries and frequencies, J. Chem. Phys. 110 (1999) 2822–2827.

[46] J.A. Montgomery, M.J. Frisch, J.W. Ochterski, G.A. Petersson, A complete basis set model chemistry VII. Use of the minimum population localized method, J. Chem. Phys. 112 (2000) 6532–6542.

[47] M.J. Frisch, G.W. Trucks, H.B. Schlegel, G.E. Scuseria, M.A. Robb, J.R. Cheeseman, G. Scalmani, V. Barone, G.A. Petersson, H. Nakatsuji, et al., Gaussian 16, Revision A.03, Gaussian, Wallingford, CT, 2016.

[48] B. Sztáray, A. Bodi, T. Baer, Modeling unimolecular reactions in photoelectron photoion coincidence experiments, J. Mass Spectrom. 45 (2010) 1233–1245.

[49] X.K. Wu, X.G. Zhou, P. Hemberger, A. Bodi, Dissociative photoionization of dimethyl carbonate: the more it is cut, the bigger the fragment ion, J. Phys. Chem. A 121 (2017) 2748–2759.

[50] O.K. Rice, H.C. Ramsperger, Theories of unimolecular reactions at low pressures, J. Am. Chem. Soc. 49 (1927) 1617.

[51] O.K. Rice, H.C. Ramsperger, Theories of unimolecular reactions at low pressures II, J. Am. Chem. Soc. 50 (1928) 617.

[52] R.A. Marcus, O.K. Rice, The kinetics of the recombination of methyl radical and iodine atoms, J. Phys. Chem. 55 (1951) 894–908.

[53] A. Bodi, M.D. Brannock, B. Sztáray, T. Baer, Tunneling in H loss from energy selected ethanol ions, Phys. Chem. Chem. Phys. 14 (2012) 16047–16054.

[54] M.F. Heringa, J.G. Slowik, A.S.H. Prevót, U. Baltensperger, P. Hemberger, A. Bodi, Dissociative ionization mechanism and appearance energies in adipic acid revealed by imaging photoelectron photoion coincidence, selective deuteration, and calculations, J. Phys. Chem. A 120 (2016) 3397–3405.

[55] Y.P. Zhu, X.K. Wu, X.F. Tang, Z.Y. Wen, F.Y. Liu, X.G. Zhou, W.J. Zhang, Synchrotron threshold photoelectron photoion coincidence spectroscopy of radicals produced in a pyrolysis source: the methyl radical, Chem. Phys. Lett. 664 (2016) 237–241.

[56] A.M. Schulenburg, C. Alcaraz, G. Grassi, F. Merkt, Rovibrational photoionization dynamics of methyl and its isotopomers studied by high-resolution photoionization and photoelectron spectroscopy, J. Chem. Phys. 125 (2006) 104310.

[57] J.A. Blush, P. Chen, R.T. Wiedmann, M.G. White, Rotationally resolved threshold photoelectron spectrum of the methyl radical, J. Chem. Phys. 98 (1993) 3557–3559.

[58] J.M. Dyke, Properties of gas-phase ions. Information to be obtained from photoelectron spectroscopy of unstable molecules, J. Chem. Soc. Faraday Trans. 2 (1987) 69 83.

[59] B. Niu, D.A. Shirley, Y. Bai, High resolution photoelectron spectroscopy and femtosecond intramolecular dynamics of H_2CO^+ and D_2CO^+, J. Chem. Phys. 98 (1993) 4377.

[60] B. Ruscic, J. Berkowitz, Photoionization mass spectrometric studies of the isomeric transient species CD_2OH and CD_3O, J. Chem. Phys. 95 (1991) 4033–4039.

[61] R.D. Johnson III, J.W. Hudgens, Structural and thermochemical properties of hydroxymethyl (CH_2OH) radicals and cations derived from observations of $B^{-2}A'(3p) \leftarrow X^{-2}A''$ electronic spectra and from ab initio calculation, J. Phys. Chem. 100 (1996) 19874–19890.

[62] K.A.G. Macneil, R.N. Dixon, High-resolution photoelectron spectroscopy of methanol and its deuterated derivatives: internal rotation in the ground ionic state, J. Electron. Spectrosc. Relat. Phenom. 11 (1977) 315–331.

[63] D. Griller, F.P. Lossing, On the thermochemistry of α-aminoalkyl radicals, J. Am. Chem. Soc. 103 (1981) 1586.

[64] P. Hemberger, J.A. van Bokhoven, J. Pérez-Ramírez, A. Bodi, New analytical tools for advanced mechanistic studies in catalysis: photoionization and photoelectron photoion coincidence spectroscopy, Catal. Sci. Technol. 10 (2020) 1975–1990.

[65] K. Ohno, K. Okamura, H. Yamakado, S. Hoshino, T. Takami, M. Yamauchi, Penning Ionization of HCHO, CH_2CH_2, and CH_2CHCHO by Collision with $He^*(2^3S)$ Metastable Atoms, J. Phys. Chem. 99 (1995) 14247–14253.
[66] X.F. Tang, X.X. Lin, G.A. Garcia, J. Loison, C. Fittschen, X.J. Gu, W.J. Zhang, L. Nahon, Threshold photoelectron spectroscopy of the methoxyl radical, J. Chem. Phys. (2020) doi:10.1063.5.0016146.
[67] S. Borkar, B. Sztaray, A. Bodi, Dissociative photoionization mechanism of methanol isotopologues (CH_3OH, CD_3OH, CH_3OD and CD_3OD) by iPEPICO: energetics, statistical and non-statistical kinetics and isotope effects, Phys. Chem. Chem. Phys. 13 (2011) 13009–13020.
[68] K. Kimura, S. Katsumata, Y. Achiba, T. Yamazaki, S. Iwata, Handbook of HeI Photoelectron Spectra of Fundamental Organic Molecules, Japan Scientific Societies, Tokyo, 1981.
[69] K. Voronova, K.M. Ervin, K.G. Torma, P. Hemberger, A. Bodi, T. Gerber, D.L. Osborn, B. Sztáray, Radical thermometers, thermochemistry, and photoelectron spectra: a photoelectron photoion coincidence spectroscopy study of the methyl peroxy radical, J. Phys. Chem. Lett. 9 (2018) 534–539.
[70] Q. Guan, K.N. Urness, T.K. Ormond, D.E. David, G. Barney Ellison, J.W. Daily, The properties of a micro-reactor for the study of the unimolecular decomposition of large molecules, Int. Rev. Phys. Chem. 33 (2014) 447–487.
[71] Z.D. Wang, X.Y. Zhang, L.L. Xing, L.D. Zhang, F. Herrmann, K. Moshammer, F. Qi, K. Kohse-Höinghaus, Experimental and kinetic modeling study of the low- and intermediate-temperature oxidation of dimethyl ether, Combust. Flame 162 (2015) 1113–1125.
[72] L. Batt, G. Alvarado-Salinas, I.A.B. ReidC, C. Robinson, D.B. Smith, The pyrolysis of dimethyl ether and formaldehyde, Symp. (Int.) Combust. 19 (1982) 81–87.
[73] Y. Hidaka, K. Sato, M. Yamane, High-temperature pyrolysis of dimethyl ether in shock waves, Combust. Flame 123 (2000) 1–22.
[74] R.X. Fernandes, C. Fittschen, H. Hippler, Kinetic investigations of the unimolecular decomposition of dimethylether behind shock waves, React. Kinet. Catal. Lett. 96 (2009) 279–289.
[75] M.N. McCabe, P. Hemberger, E. Reusch, A. Bodi, J. Bouwman, Off the beaten path: almost clean formation of indene from the *ortho*-Benzyne + Allyl reaction, J. Phys. Chem. Lett. 11 (2020) 2859–2863.
[76] C.H. Zhang, P. Li, Y.L. Li, J.N. He, X.Y. Li, Shock-tube study of dimethoxymethane ignition at high temperatures, Energy Fuels 28 (2014) 4603–4610.